processes

MDPI

Article

Research on a Fault Diagnosis Method for Rolling Bearings Based on the Fusion of PSR-CRP and DenseNet

Beining Cui, Zhaobin Tan *, Yuhang Gao, Xinyu Wang and Lv Xiao

School of Electronic and Control Engineering, North China Institute of Aerospace Engineering, Langfang 065000, China; beiningcui@163.com (B.C.); gaoyuhang0813@163.com (Y.G.); wxy20020715@163.com (X.W.); xiaolvNCIAE@163.com (L.X.)
* Correspondence: tzb@nciae.edu.cn

Abstract

To address the challenges of unstable vibration signals, indistinct fault features, and difficulties in feature extraction during rolling bearing operation, this paper presents a novel fault diagnosis method based on the fusion of PSR-CRP and DenseNet. The Phase Space Reconstruction (PSR) method transforms one-dimensional bearing vibration data into a three-dimensional space. Euclidean distances between phase points are calculated and mapped into a Color Recurrence Plot (CRP) to represent the bearings' operational state. This approach effectively reduces feature extraction ambiguity compared to RP, GAF, and MTF methods. Fault features are extracted and classified using DenseNet's densely connected topology. Compared with CNN and ViT models, DenseNet improves diagnostic accuracy by reusing limited features across multiple dimensions. The training set accuracy was 99.82% and 99.90%, while the test set accuracy is 97.03% and 95.08% for the CWRU and JNU datasets under five-fold cross-validation; *F1* scores were 0.9739 and 0.9537, respectively. This method achieves highly accurate diagnosis under conditions of non-smooth signals and inconspicuous fault characteristics and is applicable to fault diagnosis scenarios for precision components in aerospace, military systems, robotics, and related fields.

Keywords: phase space reconstruction; color recurrence plot; DenseNet; rolling bearing; fault diagnosis

check for updates

Academic Editor: Jie Zhang

Received: 1 July 2025
Revised: 21 July 2025
Accepted: 22 July 2025
Published: 25 July 2025

Citation: Cui, B.; Tan, Z.; Gao, Y.; Wang, X.; Xiao, L. Research on a Fault Diagnosis Method for Rolling Bearings Based on the Fusion of PSR-CRP and DenseNet. *Processes* **2025**, *13*, 2372. https://doi.org/10.3390/pr13082372

Copyright: © 2025 by the authors. Licensee MDPI, Basel, Switzerland. This article is an open access article distributed under the terms and conditions of the Creative Commons Attribution (CC BY) license (https://creativecommons.org/licenses/by/4.0/).

1. Introduction

During the operation of mechanical equipment, rolling bearings are frequently subjected to high-speed and heavy-load working conditions, where the operational load continuously fluctuates. Due to mechanisms such as rolling contact fatigue and material aging, these bearings are prone to various failure modes, including wear, spalling, and crack formation [1]. According to statistical data, approximately 50% of failures in rotating machinery and equipment are attributed to rolling bearings. If left undetected, minor bearing failures can lead to unplanned equipment downtime or even result in catastrophic accidents [2]. Therefore, conducting research on fault diagnosis technologies for rolling bearings holds significant scientific importance and substantial engineering application value.

Fault diagnosis technology is an interdisciplinary field characterized by strong comprehensiveness, integrating multiple disciplines including digital signal processing, machine learning, mathematical statistics, automatic control, and sensor detection [3–6]. Current fault diagnosis techniques are primarily categorized into model-based approaches [7–10]

and data-driven approaches [11–14]. While model-based methods require substantial domain expertise and extensive modeling efforts, they demonstrate effective performance in diagnosing simple faults in linear systems. However, in practical applications, systems are often nonlinear, making it challenging to establish accurate physical models, and such approaches tend to perform poorly in identifying complex and dynamic fault conditions. Data-driven fault diagnosis approaches minimize reliance on expert domain knowledge, emphasizing instead the processing of input data and the design of model architecture [15]. Gu et al. used Gramian Angular Field (GAF) to encode the vibration signals as 2D images, by using DRCNN to learn the image features and ECA to learn the correlation between the feature channels, which significantly reduced the parameters and computation while achieving an accuracy of 97.35% performance on an engine bearing dataset from a wind farm in Tianjin [16]. Guo et al. proposed a composite processing method based on GAF, Markov transition field (MTF), and the deep residual network (ResNet). They constructed a multi-channel image training set, extracted features using ResNet, and established a network framework for bearing fault classification. This integrated approach enables the network to learn more comprehensive fault features, thereby achieving improved fault recognition accuracy [17]. Wang et al. extended a one-dimensional vibration signal into a high-dimensional phase space using phase space reconstruction (PSR), fed the resulting phase diagram into a 2D-CNN, and constructed a PSR-CNN fault diagnosis model. Experimental results demonstrate that this model achieves higher accuracy and better generalization performance compared with conventional methods such as support vector machines (SVMs) and K-nearest neighbors (KNN) [18]. Jiang et al. achieved high-precision bearing fault classification by constructing a VMD-RP-CSRN diagnosis framework. In this method, the raw vibration signals were first decomposed using variational mode decomposition (VMD), then encoded into two-dimensional images through the recurrence plot (RP) technique, and finally fed into the CSRN for classification [19].

Due to bearing failure, which leads to inherently nonlinear and complex behavior, the vibration signal exhibits nonlinear characteristics, accompanied by significant noise, strong harmonic interference, and other disturbances [20,21], reflecting a chaotic state. The variation in load during operation directly influences the manifestation of bearing fault characteristics. Under zero-load conditions, the amplitude of bearing vibrations is minimal, while the noise level remains elevated. Additionally, fault pulses are weak, leading to less pronounced fault characteristics when compared to those observed under loaded conditions [22]. Furthermore, GAF may reduce the correlation between adjacent time points during coordinate mapping [23,24], potentially leading to the loss of transient features associated with early-stage faults. MTF encodes the temporal correlation of signals [25–27] by capturing state transition probabilities. This method requires discretizing continuous signals into a finite number of states. However, the amplitude variations associated with weak faults may be assigned to the same state due to inappropriately set discretization thresholds, which can result in the blurring or loss of fault characteristics. In the case of the VMD method, bearing fault features are not readily discernible under zero-load conditions. This may lead to the misclassification of weak fault features into other modal components, resulting in a reduction in the amplitude of fault features within the decomposed components. Consequently, subsequent fault feature extraction and diagnosis become more challenging. Conventional recurrence plots determine the similarity or repetition between different points in a time series by generating binarized recurrence maps based on a predefined recurrence threshold. However, this threshold is typically set empirically, which can lead to variability in the resulting recurrence patterns.

In this study, an effective fault diagnosis approach for rolling bearings is proposed based on the construction of a PSR-CRP-DenseNet model, with the following aims:

1. To address the issue of nonlinearity and poor smoothness in bearing vibration signals, one-dimensional vibration signals are extended into three-dimensional phase space using phase space reconstruction technology. This approach effectively expands the system state space and provides a more comprehensive characterization of the system's operational condition;
2. To address the issue of obscure fault characteristics in traditional recurrence plots caused by inappropriate selection of the recurrence threshold, a color recurrence diagram is employed. Specifically, the Euclidean distances between phase points in the reconstructed phase space are computed to construct a distance matrix, which is then mapped onto the Magma colormap. The continuous color transitions in this representation enhance the visibility of fault features;
3. To address the challenge of limited training samples and weak fault features, DenseNet is selected. Its densely connected topology enables efficient feature reuse and facilitates comprehensive utilization of feature information, thereby enhancing fault feature extraction and classification performance.

2. Theoretical Analysis

2.1. Phase Space Reconstruction and Color Recurrence Plot Construction (PSR-CRP)

2.1.1. Phase Space Reconstruction Theory

The Phase Space Reconstruction Theory is a fundamental approach in nonlinear time series analysis. It reveals the dynamic properties and underlying structure of the original system by embedding a one-dimensional time series into a high-dimensional phase space. The theory has attracted significant attention from scholars due to its flexible construction framework, zero-phase-shift characteristic, and effective noise reduction capability [28]. The theory of phase space reconstruction was initially introduced by Packard et al. [29] and subsequently refined by Takens et al. [30]. Takens' theorem provides the theoretical foundation for reconstructing the phase space of a dynamical system from time series data. It demonstrates that, for a deterministic dynamical system, the system's phase space can be effectively reconstructed using time-delay embedding methods, provided that the time series is sufficiently long and free of noise. A set of measurements, represented as a one-dimensional time series $x_1, x_2, x_3, \ldots x_{n-1}, x_n$, can be obtained through the observation of a nonlinear dynamical system. Phase space reconstruction maps the one-dimensional time series $x_1, x_2, x_3, \ldots x_{n-1}, x_n$ into a higher-dimensional space, thereby recovering the characteristics of the original dynamical system and revealing its features within the expanded space. This process enables the full visualization of information concealed in the one-dimensional time series, thus reconstructing the dynamic information embedded within it.

The first vector in the m-dimensional reconstruction space is formed by extracting the first N data points $X_1 = (x_1, x_2, \ldots, x_m)$, while the second vector $X_2 = (x_2, x_3, \ldots, x_{m+1})$ is generated by sequentially shifting forward with a time delay τ. Here, τ denotes the delay time interval and m represents the embedding dimension. Equation (1) represents the phase-type distribution of a one-dimensional vibration signal that has been reconstructed into an m-dimensional phase space.

$$X = \begin{bmatrix} X_1^T \\ X_2^T \\ \vdots \\ X_N^T \end{bmatrix} = \begin{bmatrix} x_1 & x_{1+\tau} & \cdots & x_{1+(m-1)\tau} \\ x_2 & x_{2+\tau} & \cdots & x_{2+(m-1)\tau} \\ \vdots & \vdots & \vdots & \vdots \\ x_N & x_{N+\tau} & \cdots & x_{N+(m-1)\tau} \end{bmatrix} \quad (1)$$

The selection of the delay time τ and the embedding dimension is crucial in the process of phase space reconstruction. Selecting an excessively small delay time parameter τ may lead to over-compression of the phase space, resulting in redundant and repetitive information [31]. Conversely, selecting an excessively large τ may cause diffusion of the phase space, a decrease in coordinate correlation, and a failure of the reconstructed phase space to accurately represent the underlying dynamical system. In the selection of the embedding dimension, it is recognized that lower dimensions, while associated with reduced computational complexity, may fail to adequately capture the system's dynamic behavior, potentially resulting in information loss. Whereas, when the embedding dimension is excessively high, although it may retain more information, it also introduces substantial redundant information, which can amplify the impact of noise and diminish the model's generalization capability. Computational complexity also constitutes a critical consideration in practical fault diagnosis tasks, particularly when processing large-scale vibration signal datasets. When the embedding dimension is relatively low, fewer computational resources and less time are required during the execution of phase space reconstruction. This enables the model to operate with greater efficiency during both training and testing phases, thereby enhancing the real-time performance and practical feasibility of the diagnostic process. The literature [32] suggests the use of an embedding parameter $\tau = 1$ and an embedding dimension m = 2 for phase space reconstruction of bearing vibration signals. However, as this study focuses on fault diagnosis under zero-load conditions, where fault characteristics are more subtle and system complexity is higher, while also considering computational efficiency, an embedding dimension of 3 is employed. This choice strikes a reasonable balance between information richness and redundancy, effectively capturing the dynamic behavior of the system without introducing excessive redundant information.

The delay time parameter τ is determined using the "mutual information" method. For two mutually independent time series $X = \{x_1, x_2, \ldots, x_m\}$ and $Y = \{y_1, y_2, \ldots, y_m\}$, the information entropy of series X and series Y can be expressed as follows, respectively:

$$H(X) = -\sum_{i=1}^{n} p(x_i) \log P(x_i) \tag{2}$$

$$H(Y) = -\sum_{j=1}^{m} p(y_i) \log P(y_i) \tag{3}$$

Let $P_{x,y}(x_i, y_i)$ denote the joint probability of x_i and y_i. Then, the joint entropy of the time series X and Y is defined as follows:

$$H(X, Y) = -\sum_{i=1}^{n} \sum_{j=1}^{m} p_{x,y}(x_i, y_i) \log P_{x,y}(x_i, y_i) \tag{4}$$

The mutual information function $I(X, Y)$ is defined as follows:

$$I(X, Y) = H(X) - H(X|Y) = H(X) + H(Y) - H(X, Y) \tag{5}$$

The mutual information measure $I(X, Y)$ quantifies the degree of interdependence between two coordinates. The degree of interdependence between two coordinates is quantified by the mutual information $I(X, Y)$, which exhibits a strong correlation and attains higher values when the delay time τ is small, gradually decreasing as τ increases. When the mutual information reaches a minimal value for the first time, it indicates that the two coordinates share the least redundant information between them, while still retaining sufficient independent information to effectively expand the phase space. The minimal value of mutual information corresponds to the maximization of independent information

between the two coordinates. This is consistent with the requirement for independent coordinates specified in the embedding theorem, thereby ensuring the validity of the phase space reconstruction. An excessively small τ leads to information redundancy, whereas an excessively large τ may introduce noise or result in information loss. The first minimal value of mutual information represents an optimal trade-off between minimizing redundancy and preserving essential information, thereby enabling the reconstructed phase space to accurately capture the underlying system dynamics. In practice, the mutual information method demonstrates robust performance across various chaotic systems, and the delay time determined by this method effectively facilitates the unfolding of phase space trajectories, thereby supporting the validity of theoretical analyses.

2.1.2. Color Recurrence Plot

Recurrence plots serve as a significant analytical tool for examining the periodicity, chaotic behavior, and non-stationarity of time series data, effectively revealing the internal structure and temporal correlations within the series. In this study, the bearing vibration signal is reconstructed into a three-dimensional time series using phase space reconstruction (PSR). By calculating the Euclidean distance between each pair of phase points, the spatial relationship within the system can be characterized. Specifically, for two points $a(x_{11}, x_{12}, \ldots, x_{1n})$ and $b(x_{21}, x_{22}, \ldots, x_{2n})$ in an n-dimensional space, the Euclidean distance is defined as follows:

$$d_{12} = \sqrt{\sum_{k=1}^{n} (x_{1k} - x_{2k})^2} \tag{6}$$

Once the Euclidean distances between all pairs of points have been computed, the distance matrix D is constructed as follows:

$$D = \begin{bmatrix} d_{n1} & d_{n2} & d_{n3} & \cdots & \cdots & d_{n(n-2)} & d_{n(n-1)} & d_{nn} \\ d_{(n-1)1} & d_{(n-1)2} & d_{(n-1)3} & \cdots & \cdots & d_{(n-1)(n-2)} & d_{(n-1)(n-1)} & d_{(n-1)n} \\ d_{(n-2)1} & d_{(n-2)2} & d_{(n-2)3} & \cdots & \cdots & d_{(n-2)(n-2)} & d_{(n-2)(n-1)} & d_{(n-2)n} \\ \vdots & \vdots & \vdots & & \iddots & \vdots & \vdots & \vdots \\ \vdots & \vdots & \vdots & \iddots & & \vdots & \vdots & \vdots \\ d_{31} & d_{32} & d_{33} & \cdots & \cdots & d_{3(n-3)} & d_{3(n-1)} & d_{3n} \\ d_{21} & d_{22} & d_{23} & \cdots & \cdots & d_{2(n-2)} & d_{2(n-1)} & d_{2n} \\ d_{11} & d_{12} & d_{13} & \cdots & \cdots & d_{1(n-2)} & d_{1(n-1)} & d_{1n} \end{bmatrix} \tag{7}$$

For different distance matrices, the color mapping thresholds in the Magma colormap corresponding to $d_{\max}$ and $d_{\min}$ are determined by traversing all elements of the distance matrix, thereby generating a color recurrence map. Magma colormap represents a continuous color gradient from black to red, and is commonly employed in data visualization to depict variations in energy levels. It was selected in this study to effectively visualize the distance relationships among phase points.

2.2. DenseNet

DenseNet is a deep learning network architecture proposed by Gao Huang et al. from Cornell University in 2017 [33]. It draws inspiration from the architectural concepts of ResNet and its predecessor, Highway Networks. DenseNet employs dense connections, whereby each layer is directly connected to all preceding layers. As a result, the input to any given layer incorporates the feature maps generated by all previous layers, in addition to its own preceding layer output, thereby enhancing feature reuse and improving the model's capacity for feature extraction. DenseNet primarily consists of dense blocks and transition layers, with the detailed architecture illustrated in Figure 1.

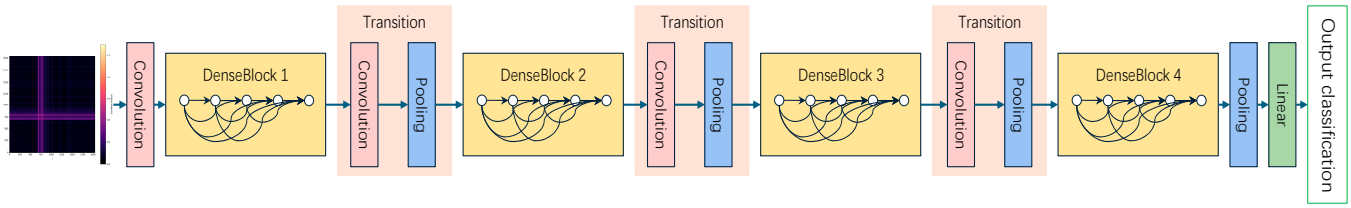


Figure 1. Architecture of DenseNet.

The dense block constitutes the core component of the network; its architectural structure is illustrated in Figure 2.

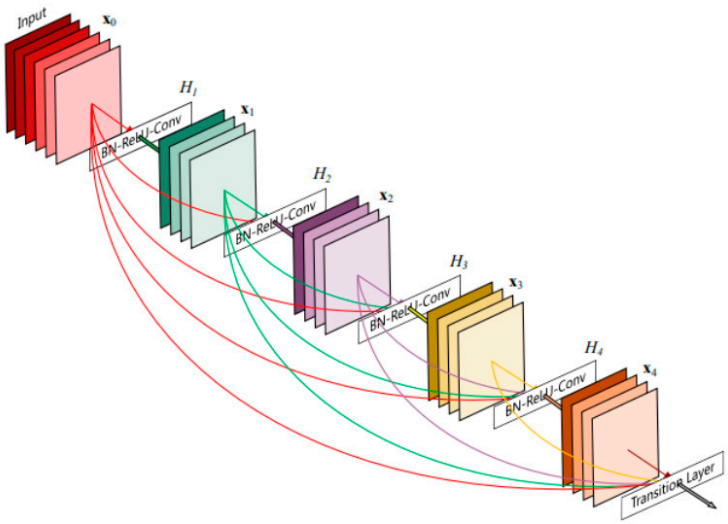


Figure 2. Model Architecture of the Dense Block.

Within the dense block, a nonlinear combination function Hi is employed to integrate the features. All feature maps generated prior to layer i, such as $X_0, X_1, X_2, \ldots, X_{i-1}$, are obtained through a sequence of operations including batch normalization (BN), ReLU activation, and convolution (Conv). These feature maps are then used as inputs to layer i, denoted as:

$$X_i = H_i([X_0, X_1, \ldots, X_{i-1}]) \tag{8}$$

The Transition layer is positioned between two adjacent Dense Blocks. It consists of a convolutional layer (1×1) and an average pooling layer (2×2), serving a critical role in connectivity, dimensionality reduction, and performance enhancement. This design enables the network to achieve stronger feature extraction capabilities and improved training efficiency while preserving its depth.

2.3. Model Evaluation Methodology

For fault diagnostic models, the primary evaluation metrics include accuracy, precision, recall, and *F1* score. Accuracy reflects the proportion of samples that are correctly classified:

$$ACC = \frac{TP + TN}{TP + TN + FP + FN} \tag{9}$$

Precision reflects the proportion of samples predicted to belong to a given class that are correctly classified into that class:

$$P = \frac{TP}{TP + FP} \tag{10}$$

Recall reflects the proportion of all fault samples that are accurately classified into a specific fault category:

$$R = \frac{TP}{TP + FN} \tag{11}$$

The *F1* score represents a weighted harmonic mean of precision and recall:

$$F_1 = \frac{2PR}{P + R} \tag{12}$$

The number of samples for which the positive class is correctly predicted is denoted as *TP* (true positive); the number of samples for which the negative class is correctly predicted is denoted as *TN* (true negative); the number of samples for which the negative class is incorrectly predicted as positive is denoted as *FP* (false positive); and the number of samples for which the positive class is incorrectly predicted as negative is denoted as *FN* (false negative). In this study, accuracy and the *F1* score are utilized as evaluation metrics, with values ranging from 0 to 1. A higher score signifies superior model performance in terms of accuracy, precision, and recall, rendering it an effective and intuitive measure for assessing overall model efficacy.

3. Experimental Data

3.1. CWRU Public Datasets

In this study, the CWRU public dataset is utilized for data preprocessing and model training. The CWRU dataset, provided by Case Western Reserve University in the United States, is a publicly accessible collection of bearing vibration data. The experimental testbed of the CWRU dataset is illustrated in Figure 3. The dataset employs accelerometers to collect vibration data from motor bearings under various fault conditions and load levels at a sampling frequency of 12 kHz. Bearing defect locations encompass failures of the rolling elements, inner ring, and outer ring. As illustrated in Table 1, multiple fault defect sizes from the CWRU dataset were selected for this study, with 0 load applied to the fan-end data. The classification categories include normal (label 0), inner ring fault (label 1), outer ring fault (label 2), and rolling element fault (label 3).

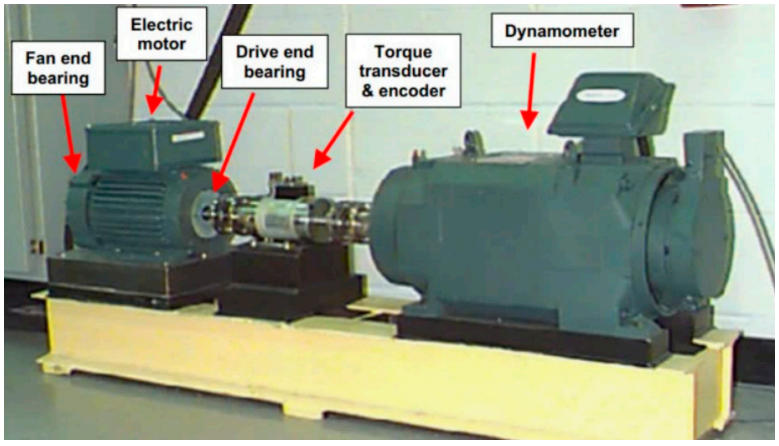
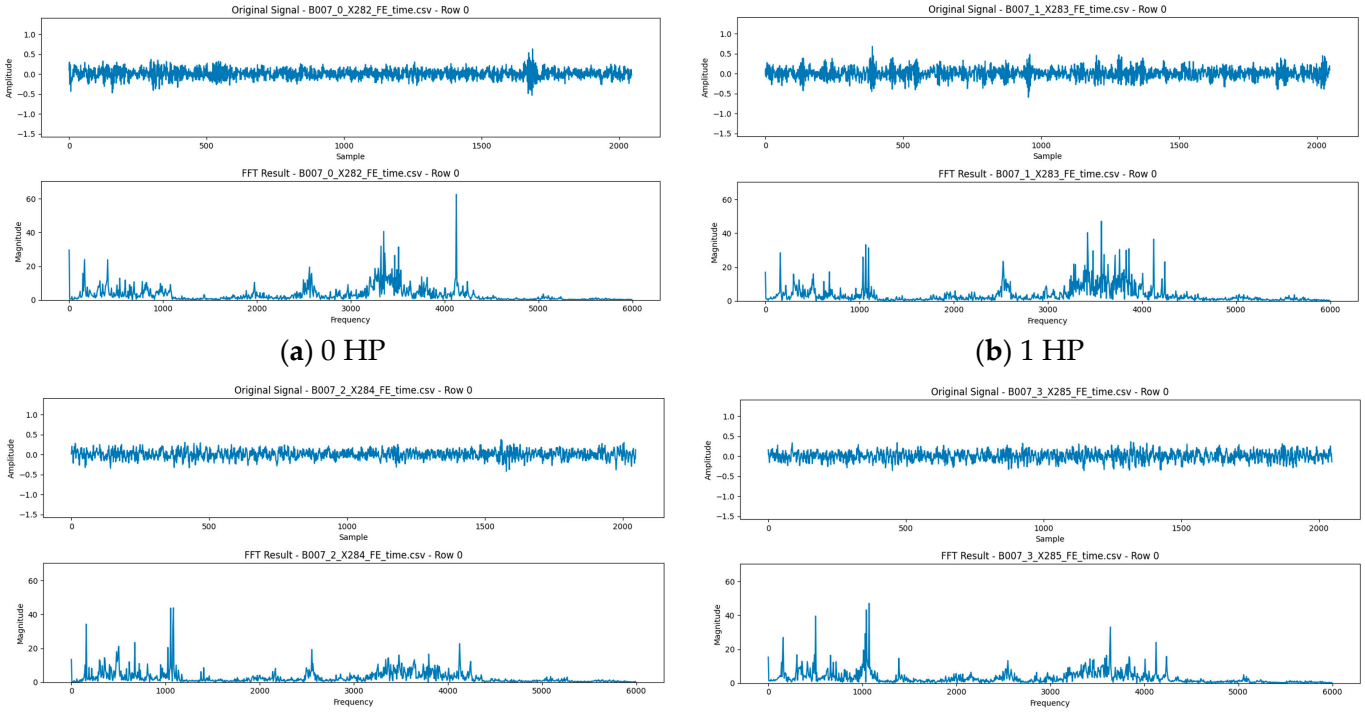


Figure 3. CWRU Dataset Pilot Testbed.

Under zero-load conditions, the vibration caused by rolling element faults is insufficiently constrained, leading to the dispersion of vibration energy across multiple frequency components. In the frequency domain, although certain frequency components may be present, distinct fault characteristic frequencies are not clearly identifiable. This makes it challenging to extract meaningful fault features from complex vibration signals and increases the difficulty of fault diagnosis. Zero-load conditions represent the scenario in

which fault characteristics are least pronounced. In real industrial environments, bearing failures typically present as weak fault signals during their early stages, particularly under low-load operating conditions. These weak fault signals are frequently obscured by noise and external disturbances, presenting a considerable challenge to fault diagnosis. As illustrated in Figure 4, the raw waveforms acquired under various load conditions for a rolling element fault (with a fault size of 0.007 inches) are represented in the frequency domain at the corresponding sampling frequency of 12 kHz. In the frequency domain representation, although certain frequency components are present, no distinct fault characteristic frequency can be clearly identified, which makes it challenging to recognize fault features effectively within complex vibration signals. Under higher load conditions (e.g., 1 HP, 2 HP, 3 HP), the internal contact stiffness and constraint of the bearing increase. Bearing failures are more evident in the lower frequency band (0–1000 Hz), where the amplitude of certain low-frequency components increases. This leads to a more pronounced low-frequency vibration response, thereby enhancing the detectability of the fault signature. In such cases, even conventional diagnostic methods can achieve relatively high diagnostic accuracy, which fails to sufficiently demonstrate the effectiveness of the proposed method. The weakest fault characteristics observed under the zero-load condition more accurately represent the weak fault signal scenario of a bearing in its early failure stage. Therefore, the bearing vibration signal under zero load condition was selected in this study to facilitate the validation of the feasibility and effectiveness of the proposed method in practical applications.



(**a**) 0 HP (**b**) 1 HP

(**c**) 2 HP (**d**) 3 HP

Figure 4. Time and Frequency Domain Representations of Rolling Body Faults under Different Load Conditions (Fault Size: 0.007 Inches).

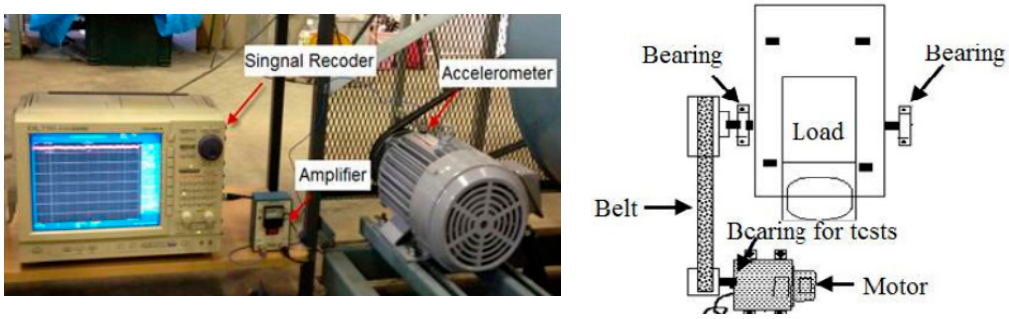
Table 1. Bearing Fault Classification Information from the CWRU Dataset.

Type	Fault Size	Number of Samples	Number of Labels	Label	Load	Sampling Rate
Normal		119	119	N (0)	0 HP	12 KHz
Inner Ring Fault	0.007″ 0.014″ 0.021″	59 59 59	177	I (1)		
Outer Ring Fault	0.007″ 0.014″ 0.021″	118 59 58	236	O (2)		
Rolling Element Fault	0.007″ 0.014″ 0.021″	59 59 59	177	B (3)		

0.007 inches is abbreviated as 0.007″.

3.2. Jiangnan University Dataset

To validate the performance of the proposed model, a subset of the Jiangnan University bearing dataset was selected for testing. Figure 5 illustrates the bearing test platform and mechanism schematic of Jiangnan University. The testbed consisted of a fault diagnosis setup for a centrifugal fan system driven by a Mitsubishi SB-JR induction motor. The motor is a 3.7 kW three-phase induction motor with a voltage rating of 220 V, four poles, a rated speed of 1800 rpm, and a rotor supported by two bearings. As illustrated in Table 2, the bearing vibration data at 800 rpm and 1000 rpm for normal conditions, inner ring faults, outer ring faults, and rolling element faults were selected for testing in this study.



(**a**) Bearing Test Platform (**b**) Mechanism Schematic

Figure 5. Bearing Test Platform (**a**) and Mechanism Schematic (**b**).

Table 2. Bearing Fault Classification Information from the JNU Dataset.

Type	Rotational Speed	Fault Size (Width × Depth)	Number of Samples	Number of Labels	Label	Sampling Rate
Normal	800 rpm 1000 rpm		41 41	82	N (0)	50 KHz
Inner Ring Fault	800 rpm 1000 rpm	0.3 × 0.25 mm	30 30	60	I (1)	
Outer Ring Fault	800 rpm 1000 rpm	0.3 × 0.25 mm	30 30	60	O (2)	
Rolling Element Fault	800 rpm 1000 rpm	0.5 × 0.15 mm	30 30	60	B (3)	

4. Fault Diagnosis

4.1. Signal Processing

The CWRU public dataset was collected at a sampling frequency of 12 kHz and an approximate rotational speed of 1800 rpm. At CWRU, the raw signal was initially divided into segments containing 2048 data points each. Let the sampling frequency be denoted as f_s, the number of sampling points as N, the time window as T, and the rotational speed of the device as n, then the number of revolutions c made by the device within a time window T can be expressed as follows:

$$c = T \times \frac{n}{60} = \frac{N}{f_s} \times \frac{n}{60} \tag{13}$$

Through data substitution, it can be determined that there are approximately five rotational cycles within a time window T. When the data is grouped into segments of 2048 sampling points, multiple fault points across the operational phases of the bearings are covered. This ensures that the dataset contains relevant information regarding bearing faults. To achieve more reliable experimental results, the experimental data should be normalized using the following normalization formula:

$$X_{normalized} = \frac{X - X_{\min}}{X_{\max} - X_{\min}} \tag{14}$$

where X represents the original data point, $X_{\min}$ denotes the minimum value in the signal sequence, and $X_{\max}$ denotes the maximum value in the signal sequence.

Taking the data of a bearing operation from the CWRU public dataset as an example, the normalized vibration signals were embedded into a high-dimensional phase space through the application of phase space reconstruction (PSR) technique. In this study, m = 3 was selected for phase space reconstruction, while the delay time parameter was determined using the "mutual information" method, and the candidate range of delay time τ was set to $[1, 200]$. The reconstructed signal was transformed into a Magma chromatic diagram, resulting in the generation of a recurrence plot through the calculation of Euclidean distances between each pair of phase points. Figure 6 presents a recurrence plot of a specific faulty bearing from the CWRU public dataset.

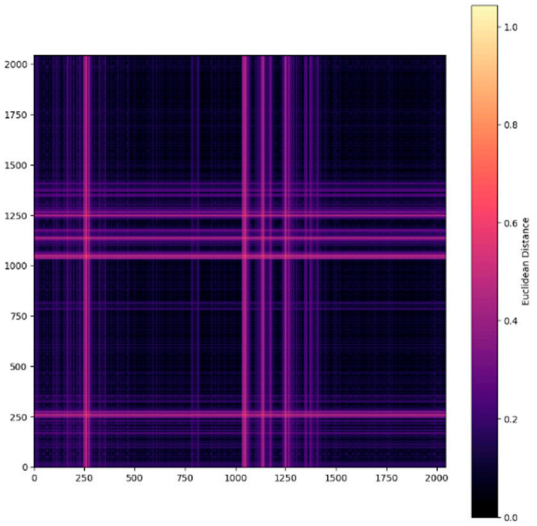


Figure 6. Color recurrence plot of a specific failed bearing from the CWRU public dataset.

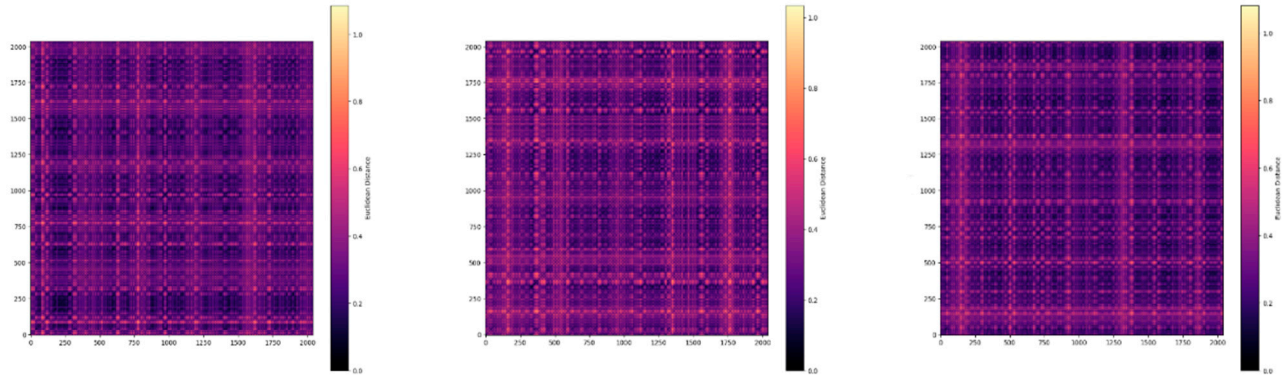
4.2. Comparison of Recurrence Plots Among Different Fault Types

In this study, the types of bearing failures examined include rolling element failures, inner ring failures, and outer ring failures. The visualization results of randomly selected normal, rolling element failure, inner ring failure, and outer ring failure samples using PSR-CRP are presented in Figure 7. The recurrence plot of the normal bearing exhibits a relatively dense and uniformly distributed grid-like structure, with a clear diagonal pattern extending from the upper left to the lower right. Additionally, numerous parallel subordinate diagonal structures are observed, predominantly in purple, with only a few regions displaying red hues. This indicates that the vibration signal of the normal bearing is highly regular, with small Euclidean distances between phase points, suggesting a stable operational state. The vibration pattern demonstrates high repeatability and predictability. When comparing the recurrence plots of the three faulty bearings, it can be observed that the distribution of high-density regions in their recurrence plots is relatively sparse. The grid-like structure becomes blurred or even fragmented, while diagonal and subordinate diagonal features are less distinct compared to those of the normal bearing. Additionally, the color distribution exhibits greater complexity, characterized by an increased presence of dark-colored regions and localized red areas. This indicates that the regularity of the faulty bearing's vibration signal is compromised, the Euclidean distances between phase points are non-uniformly distributed, the system stability is reduced, and abnormal vibration patterns along with unpredictable dynamic behaviors emerge.

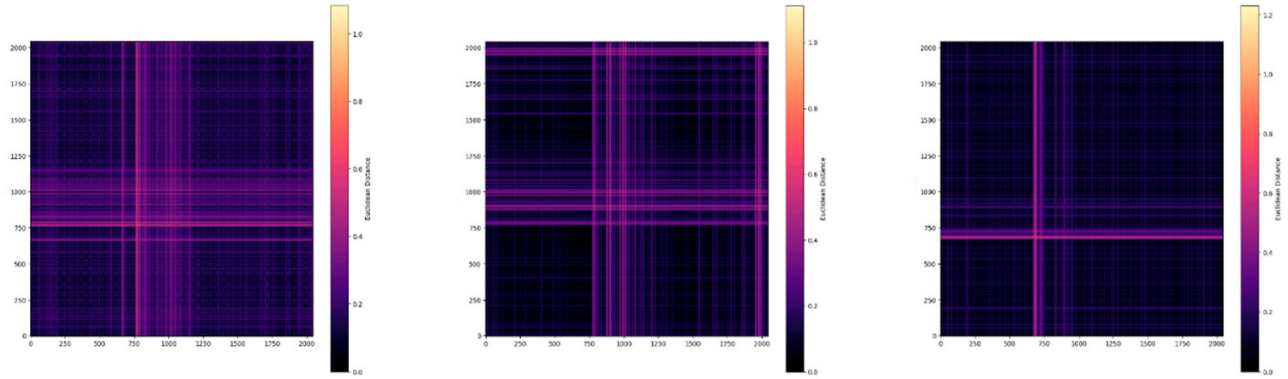
The distribution of bright spots in the CRP of the rolling element failure exhibits distinct irregular patterns characterized by horizontal and vertical line crossings. The positions of these lines are relatively dispersed, with variable spacing between them. Certain regions display higher line density, and the color transition between purple and black is more pronounced. This may be attributed to the fact that rolling element failure induced by localized shock and vibration results in greater disturbances, leading to more pronounced changes in phase points at specific positions. These disturbances subsequently affect the distribution characteristics of the recurrence plot, reflecting the significant local impact of rolling element failure on the bearing's vibration signal.

Although the grid-like structure in the distribution of bright spots within the CRP diagram of the inner ring failure is still present, it becomes increasingly twisted and distorted. The lines are no longer straight and parallel as observed in normal bearings, exhibiting more bends and interlacing patterns. Furthermore, the color distribution demonstrates greater complexity. Failure of the inner ring induces significant alterations in the internal force distribution and vibration pattern of the bearing. As reflected in the recurrence plot, this manifests as irregular structural distortions, indicating changes in both the frequency and amplitude characteristics of the bearing's vibration signal.

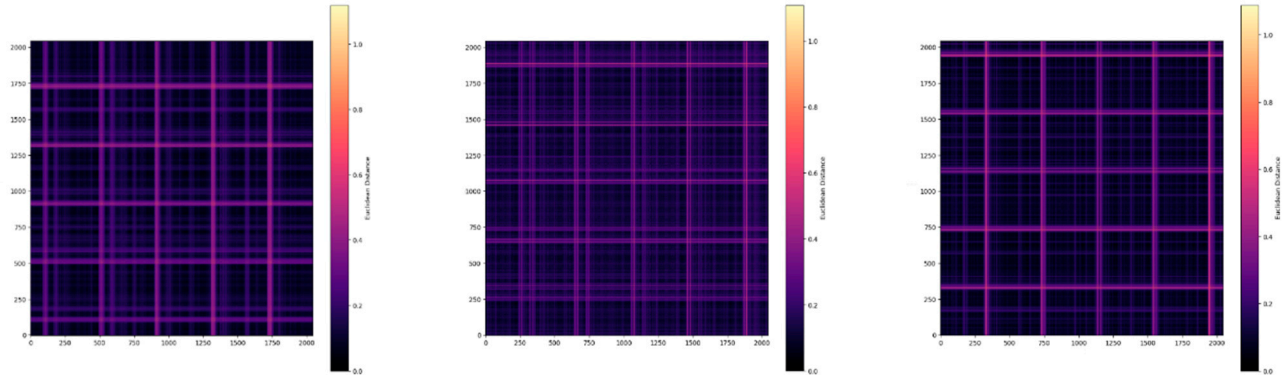
The distribution of high-density regions in the CRP maps of outer ring faults exhibits a more distinct chevron-like pattern formed by intersecting vertical and horizontal lines. The lines appear darker, display higher contrast relative to the background, and the color distribution is predominantly concentrated between purple and black. The influence of outer ring failure is primarily manifested in directional variations of the vibration characteristics. As observed in the recurrence plot, this is represented by more structured vertical and horizontal line patterns, indicating that the outer ring failure has introduced greater disruption to the regularity of the bearing's vibration signals in specific directions. This results in notable alterations in the Euclidean distances of phase points along those directions, ultimately leading to the formation of a distinct chevron-like pattern.



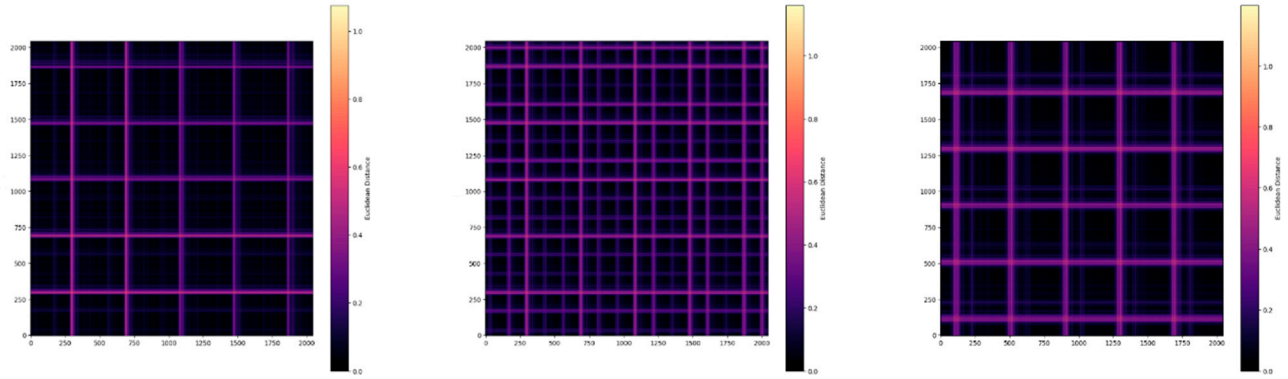
(**a**) normal



(**b**) Rolling faults



(**c**) Inner ring failure



(**d**) Outer ring failure

Figure 7. Colored Recurrence Plots of the Normal and Three Fault Conditions of the Bearing Using PSR.

In summary, the differences observed in the 3D phase space reconstruction maps between normal bearings and three types of faulty bearings can serve as feature inputs for a classification model to distinguish among various fault categories. This finding theoretically confirms the feasibility of employing visual methods for bearing fault diagnosis and provides a theoretical foundation for the subsequent development of the PSR-RP-DenseNet fault diagnosis model.

4.3. PSR-RP-DenseNet Diagnostic Model

In this study, the fault diagnosis of rolling bearings was accomplished through the construction of a PSR-CRP-DenseNet model. The overall architecture of the diagnostic framework is illustrated in Figure 8.

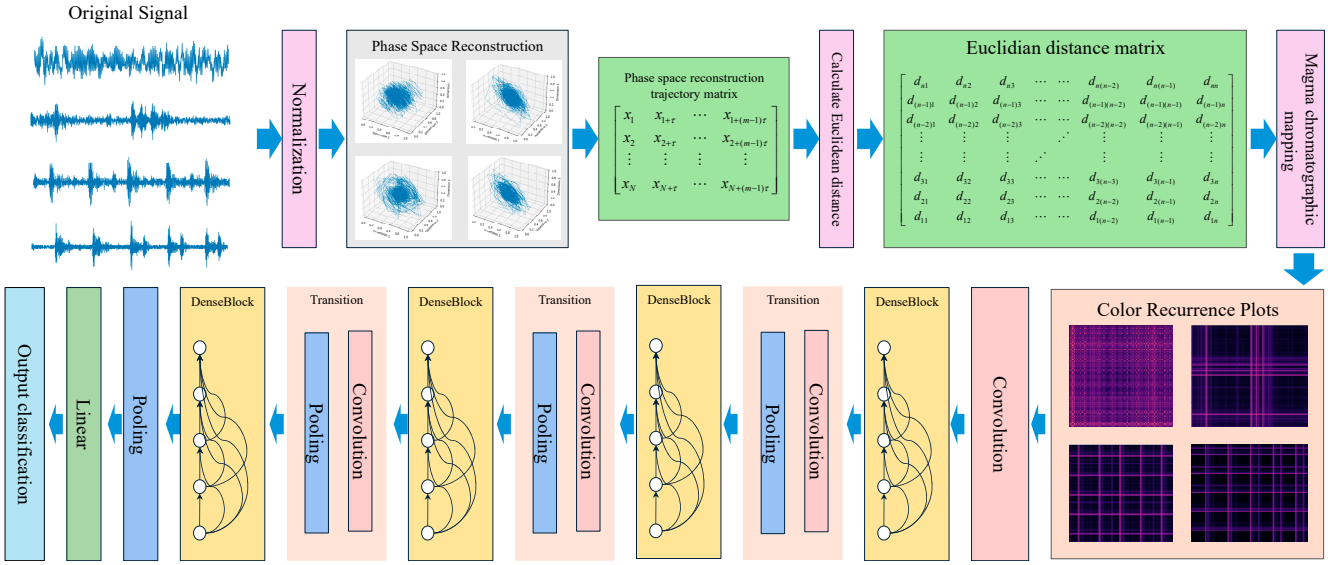


Figure 8. Overall Architecture of the PSR-CRP-DenseNet Diagnostic Framework.

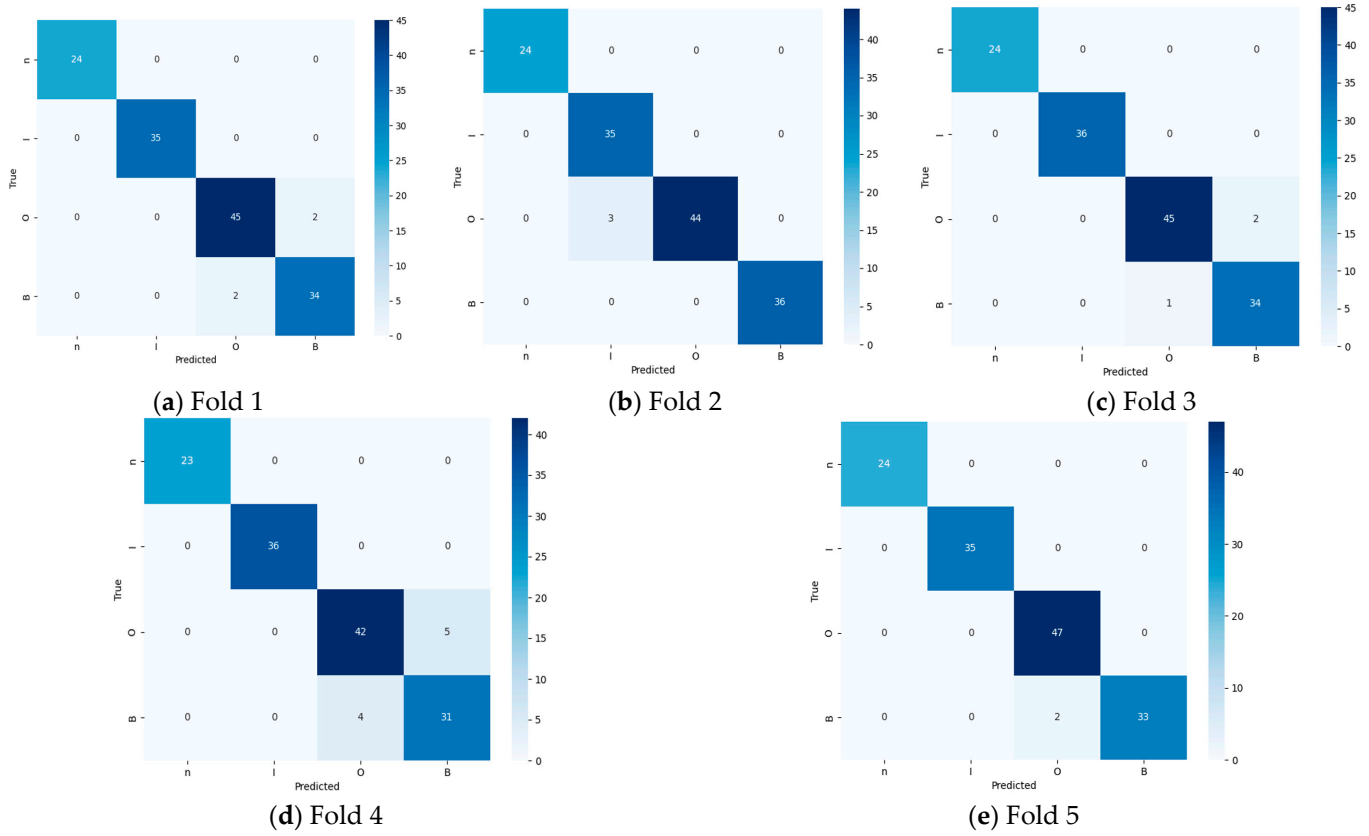
The bearing vibration signal was reconstructed through PSR to expand the one-dimensional vibration signal into a three-dimensional phase space, thereby providing a more comprehensive characterization of the system's operational state. The Euclidean distance between each pair of phase points was computed and subsequently mapped into the Magma colormap to generate a colored recurrence map, which was then fed into DenseNet for fault classification. The DenseNet model employed in this study was DenseNet-121; the detailed architectural parameters are summarized in Table 3.

Table 3. DenseNet Network Parameters.

Parameter	Value
growth_rate	32
block_config	(6, 12, 24, 16)
drop_rate	0.6
num_classes	4
num_epochs	100
learning_rate	0.0001
batch_size	32

To mitigate performance variations caused by dataset partitioning, this study employed five-fold cross-validation. Each fold involved 100 training epochs, resulting in an average training accuracy of 99.82%, a validation accuracy of 97.03%, and an *F1* score of 0.9739. In Figure 9, the confusion matrix of the proposed method in this study on the

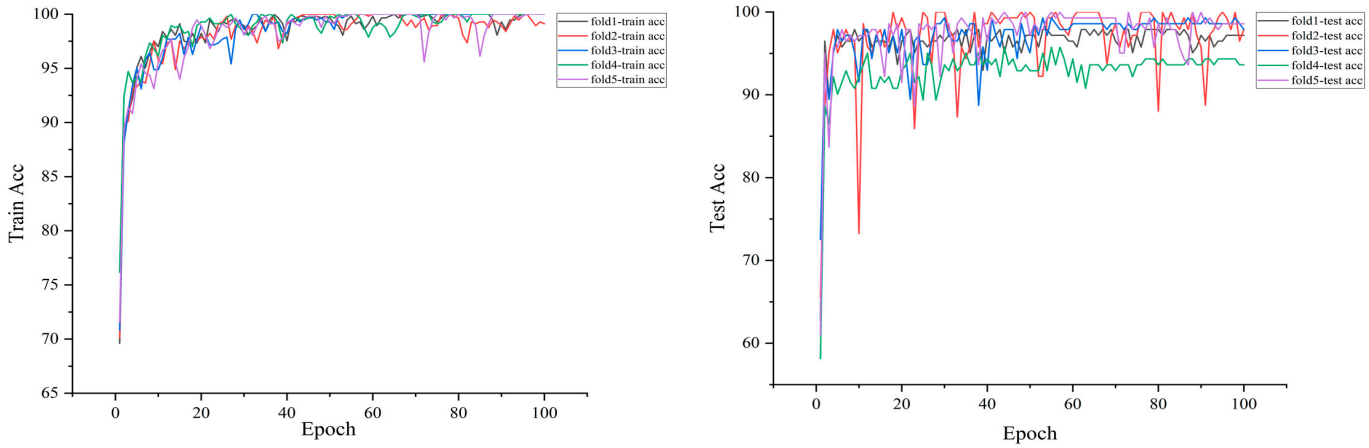
CWRU dataset is presented. Figure 10 displays the variation curves of the loss function with respect to the training and test sets.



(**a**) Fold 1 (**b**) Fold 2 (**c**) Fold 3

(**d**) Fold 4 (**e**) Fold 5

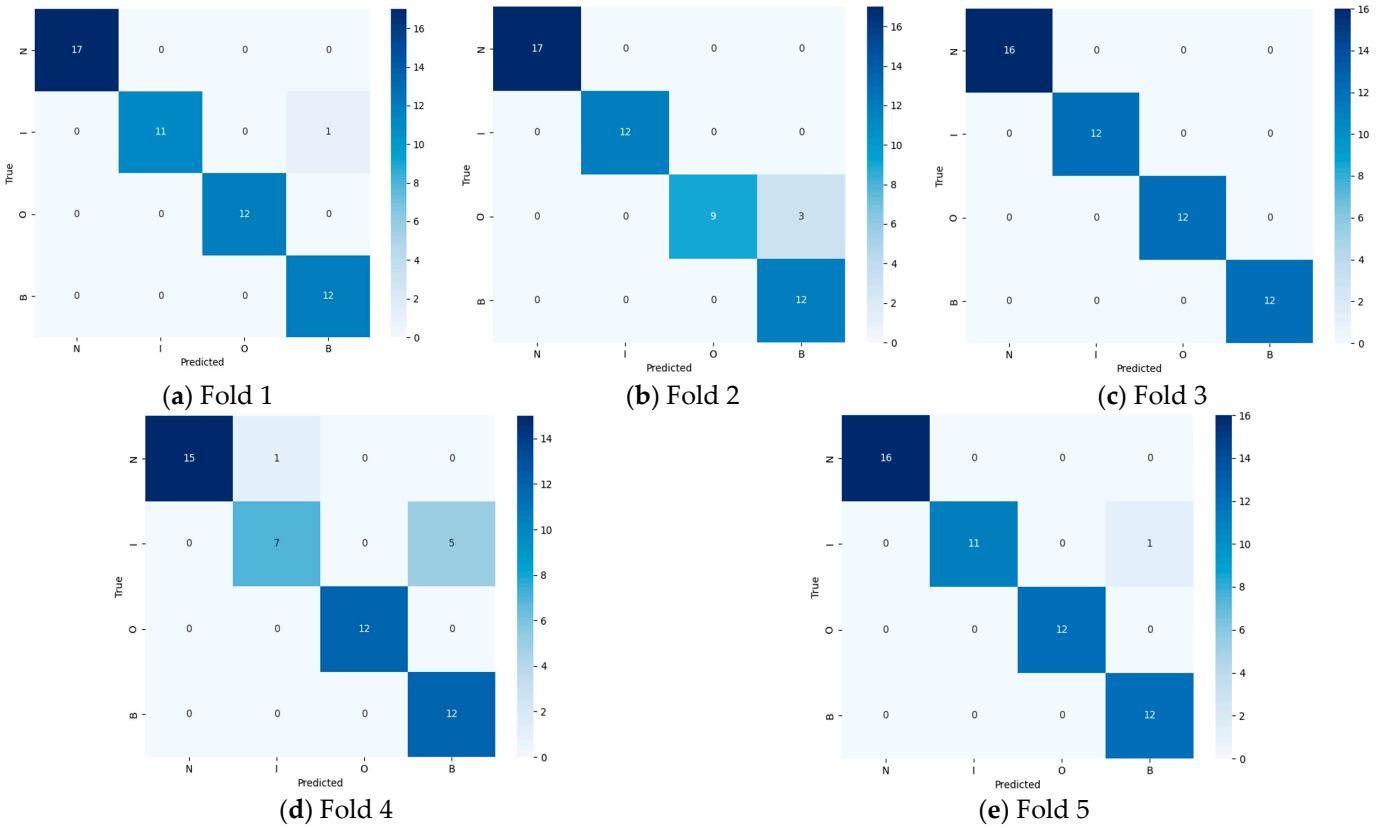
Figure 9. Confusion Matrix of Five-Fold Cross-Validation on the CWRU Bearing Dataset.



(**a**) Train Acc (**b**)Test Acc

Figure 10. Accuracy Variation Curves of the Training (**a**) and Testing (**b**) Sets.

To further validate the model performance, the proposed approach in this study was subjected to five-fold cross-validation on the Jiangnan University bearing dataset. The results demonstrated an average accuracy of 99.9%, a test set average accuracy of 95.08%, and an *F1* score of 0.9537. Notably, the classification accuracy reached 100% on the test set during the third fold, indicating the model's strong generalization capability. Figure 11: Five-Fold Cross-Validation Confusion Matrix on the JNU Bearing Dataset



(**a**) Fold 1 (**b**) Fold 2 (**c**) Fold 3

(**d**) Fold 4 (**e**) Fold 5

Figure 11. Confusion Matrix of Five-Fold Cross-Validation on the JNU Bearing Dataset.

4.4. Comparison with Other Diagnostic Models

To verify the effectiveness of the proposed method, a comparative evaluation was conducted against existing classification models (CNN, ViT, VGG, ResNet) and signal processing algorithms, as illustrated in Table 4 and Figure 12. The experiments were performed using five-fold cross-validation, with a dropout rate set to 0.6, input image dimensions of (224, 224), and 100 training epochs per fold.

Table 4. Test Results of Different Models.

Serial	Model	Average Train Acc	Average Test Acc	*F1* Score	Test Accuracy Improvement	*F1* Score Improvement
1	MTF-DenseNet	99.33%	92.51%	0.9328	4.52%	0.041
2	GAF-DenseNet	99.79%	96.47%	0.9689	0.56%	0.005
3	PSR-CRP-CNN	88.91%	90.53%	0.9110	6.5%	0.063
4	PSR-CRP-ViT	88.60%	69.49%	0.6966	27.54%	0.277
5	PSR-CRP-VGG	98.94%	93.22%	0.9398	3.81%	0.034
6	PSR-CRP-ResNet	99.01%	92.09%	0.9283	4.94%	0.046
7	PSR-CRP-DenseNet	99.82%	97.03%	0.9739		

To validate the effectiveness of signal processing in the proposed method, this study compared two classical algorithms—MTF-DenseNet and GAF-DenseNet—that convert one-dimensional vibration signals into two-dimensional images. MTF captures the temporal correlation of signals by utilizing state transition probabilities. However, during the discretization of continuous signals into finite states, amplitude variations associated with weak faults may be assigned to the same state if the discretization thresholds are not appropriately set, resulting in a loss or blurring of fault characteristics. In contrast, GAF reduces the correlation between adjacent time points during coordinate mapping.

The method proposed in this study effectively preserves and reflects both the correlation and dynamic changes among phase points in the phase space. Following five-fold cross-validation, the PSR-CRP approach proposed in this study achieved average test set accuracy improvements of 4.52% and 0.56%, as well as *F1* score enhancements of 0.041 and 0.005, respectively, compared with MTF and GAF. These results demonstrate the effectiveness and superiority of the proposed signal processing method.

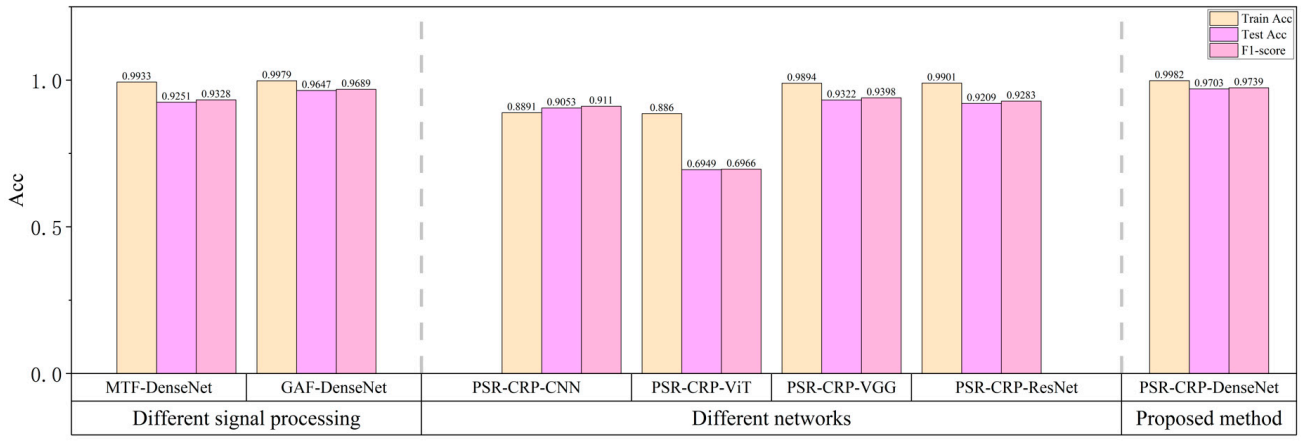


Figure 12. Test Results of Different Models.

Regarding the superiority of the feature extraction network in the proposed method, PSR-CRP-CNN, PSR-CRP-ViT, PSR-CRP-VGG, and PSR-CRP-ResNet employ phase space reconstruction to generate color recurrence plots for signal processing. This approach transforms one-dimensional vibration signals into two-dimensional color images but utilizes different subsequent feature extraction networks compared to the method presented in this study. Following five-fold cross-validation, the DenseNet network demonstrated average test set accuracy improvements of 6.5%, 27.54%, 3.81%, and 4.94%, as well as *F1* score enhancements of 0.063, 0.277, 0.034, and 0.046, respectively, compared with the CNN, ViT, VGG, and ResNet networks. These results clearly indicate that, even with a limited training dataset, DenseNet effectively leverages dense connectivity to fully extract and learn features, thereby achieving superior performance in terms of both classification accuracy and *F1* score for fault diagnosis.

5. Conclusions

In this paper, a bearing fault diagnosis model based on the fusion of PSR-CRP and DenseNet is proposed. This section presents a summary and outlook of the research work.

Regarding on-smooth signal processing, considering the non-smooth characteristics of rolling bearing vibration signals and the fact that weak fault features are not readily discernible, the phase space reconstruction method is employed to process one-dimensional vibration signals. The optimal delay time is determined using the mutual information method, and the signal is subsequently extended into three-dimensional phase space. The experimental results demonstrate that the delay time parameter obtained through the mutual information method effectively balances the elimination of redundant information with the preservation of critical dynamic information, thereby enabling the reconstructed phase space to accurately represent the system's dynamic characteristics.

To mitigate the feature blurring issue that may occur during feature extraction with conventional methods such as RP and GAF, an enhanced feature visualization technique based on CRP is proposed. The method generates color CRP maps by computing the Euclidean distances of phase points in a high-dimensional space and mapping these

distances to the Magma colormap, thereby providing richer texture and color information for the feature extraction network and enhancing feature separability.

For efficient feature extraction and classification during the feature extraction phase, DenseNet with a densely connected topology is employed as the classifier. The network exhibits robust feature extraction and classification capabilities in small-sample scenarios, and enables precise identification of weak fault features through efficient feature reuse. Experimental results indicate that DenseNet achieved satisfactory performance on the CWRU and JNU datasets.

With regard to the model's comparitive advantage, compared with models such as MTF-DenseNet and GAF-DenseNet, the proposed method demonstrated improvements in test set accuracy and *F1* score, thereby validating the effectiveness of signal processing approaches in preserving feature information. Meanwhile, compared with different feature extraction networks such as CNN, ViT, VGG, and ResNet, DenseNet demonstrated enhanced performance in both classification accuracy and *F1* score, indicating its superior capability in feature extraction.

Future research will primarily focus on the following aspects:

(1) The currently utilized dataset does not encompass all practical application scenarios. Future work will focus on expanding the dataset to incorporate various types of bearings, diverse operating conditions (e.g., varying loads, speeds, and temperatures), and multiple failure modes. This enhancement is expected to strengthen the model's generalization capability and adaptability;

(2) Multimodal feature fusion strategies should be investigated, integrating multi-source information such as rotational speed, temperature, and load into the deep learning model, and design a multi-input network architecture to enable collaborative utilization of multi-dimensional features. Meanwhile, attention should be given to the sampling frequency synchronization across different modalities to avoid bias in multimodal feature fusion caused by temporal domain discrepancies;

(3) Further optimization of the model structure can reduce its complexity and enhance the model's real-time inference capability, thereby better meeting the practical requirements of online monitoring and fault diagnosis. The application of the optimized model might be extended to a broader range of industrial scenarios to validate its stability and adaptability across diverse operating conditions.

Author Contributions: Conceptualization, B.C., Z.T. and Y.G.; Methodology, Z.T., B.C. and L.X.; Software, B.C., Y.G. and X.W.; Validation, B.C. and Z.T.; Formal analysis, L.X.; Investigation, B.C., X.W. and L.X.; Resources, Z.T.; Data curation, B.C. and X.W.; Writing—original draft, B.C.; Writing—review & editing, Z.T.; Visualization, B.C. and Y.G.; Supervision, Z.T. All authors have read and agreed to the published version of the manuscript.

Funding: This research was funded by North China Institute of Aerospace Engineering, grant number YKY-2024-23.

Data Availability Statement: The original data presented in the study are openly available at https://engineering.case.edu/bearingdatacenter (accessed on 1 February 2025, CWRU dataset) and https://gitcode.com/Resource-Bundle-Collection/ac90f (accessed on 1 February 2025, JNU dataset).

Conflicts of Interest: The authors declare no conflicts of interest.

References

1. Zhang, J.; Wu, J.; Hu, B.; Tang, J. Intelligent fault diagnosis of rolling bearings using variational mode decomposition and self-organizing feature map. *J. Vib. Control* **2020**, *26*, 1886–1897. [CrossRef]
2. Rai, A.; Upadhyay, S.H. A review on signal processing techniques utilized in the fault diagnosis of rolling element bearings. *Tribol. Int.* **2016**, *96*, 289–306. [CrossRef]

3. Zhang, B.; Wang, W.; He, Y. A hybrid approach combining deep learning and signal processing for bearing fault diagnosis under imbalanced samples and multiple operating conditions. *Sci. Rep.* **2025**, *15*, 13606. [CrossRef] [PubMed]
4. Chandrvanshi, S.; Sharma, S.; Singh, M.P.; Singh, R. Bearing Fault Diagnosis Using Machine Learning Models. In Proceedings of the International Conference on Micro-Electronics and Telecommunication Engineering, Ghaziabad, India, 22–23 September 2023; Springer Nature: Singapore, 2023; pp. 219–233.
5. Nie, Y.; Li, F.; Wang, L.; Li, J.; Li, Y.; Sun, M.; Wang, M.; Li, G. A novel vibration model for explanation of the frequency features in multistage wind turbine gearboxes considering the effects of inter-stage meshing frequency modulation. *Int. J. Precis. Eng. Manuf.-Green Technol.* **2023**, *10*, 151–166. [CrossRef]
6. Satish, C.R.; Kilmer, K.R.; Jiang, J.; Zhou, X.; Tan, L. Deep Learning Based Bearing Fault Detection Using Multi-Rate Signal Processing for Regulating Shaft Rotational Speed. In Proceedings of the SoutheastCon 2025, Concord, NC, USA, 22–30 March 2025; pp. 390–395.
7. Zheng, L.; Xiang, Y.; Luo, N. Nonlinear dynamic modeling and vibration analysis for early fault evolution of rolling bearings. *Sci. Rep.* **2024**, *14*, 23687. [CrossRef]
8. Zhang, R.; Guo, L.; Zong, Z.; Gao, H.; Qian, M.; Chen, Z. Dynamic modeling and analysis of rolling bearings with rolling element defect considering time-varying impact force. *J. Sound Vib.* **2023**, *562*, 117820. [CrossRef]
9. Otava, L.; Buchta, L. Permanent magnet synchronous motor stator winding fault detection. In Proceedings of the IECON 2016-42nd Annual Conference of the IEEE Industrial Electronics Society, Florence, Italy, 23–26 October 2016; IEEE: Piscataway, NJ, USA, 2016; pp. 1536–1541.
10. Zeng, C.; Huang, S.; Lei, J.; Wan, Z.; Yang, Y. Online Rotor Fault Diagnosis of Permanent Magnet Synchronous Motors Based on Stator Tooth Flux. *IEEE Trans. Ind. Appl.* **2021**, *57*, 2366–2377. [CrossRef]
11. Surendran, R.; Khalaf, O.I.; Tavera Romero, C.A. Deep learning based intelligent industrial fault diagnosis model. *Comput. Mater. Contin.* **2022**, *70*, 6323–6338. [CrossRef]
12. Yin, C.; Lee, H.P.; Ko, J.H.; Wang, Y. Intelligent Fault Diagnosis of Rolling Bearings in Strong Noise Environment: An Attention-Driven Hybrid Model Based on IENEMD and Parallel Multiscale CNN. *Int. J. Precis. Eng. Manuf.-Green Technol.* **2025**, *12*, 1091–1116. [CrossRef]
13. Wei, L.; Peng, X.; Cao, Y. Intelligent fault diagnosis of rolling bearings in strongly noisy environments using graph convolutional networks. *Int. J. Adapt. Control Signal Process.* **2024**, *39*, 1469–1482. [CrossRef]
14. Saha, D.K.; Hoque, M.E.; Badihi, H. Development of Intelligent Fault Diagnosis Technique of Rotary Machine Element Bearing: A Machine Learning Approach. *Sensors* **2022**, *22*, 1073. [CrossRef]
15. Lei, L.; Li, W.; Zhang, S.; Wu, C.; Yu, H. Research Progress on Data-Driven Industrial Fault Diagnosis Methods. *Sensors* **2025**, *25*, 2952. [CrossRef]
16. Gu, X.; Xie, Y.; Tian, Y.; Liu, T. A Lightweight Neural Network Based on GAF and ECA for Bearing Fault Diagnosis. *Metals* **2023**, *13*, 822. [CrossRef]
17. Guo, L.; Zhang, L.; Huang, Q. Bearing Fault Diagnosis Based on Multi-Channel GAF-MTF and Res2Net. In Proceedings of the 2023 35th Chinese Control and Decision Conference (CCDC), Yichang, China, 20–22 May 2023; IEEE: Piscataway, NJ, USA, 2023; pp. 5321–5327.
18. Mengjiao, W.; Liting, D. A new fault diagnosis of rolling bearing based on phase-space reconstruction and convolutional neural network. *Ind. Lubr. Tribol.* **2023**, *75*, 875–882. [CrossRef]
19. Jiang, Y.; Xie, J. VMD–RP–CSRN Based Fault Diagnosis Method for Rolling Bearings. *Electronics* **2022**, *11*, 4046. [CrossRef]
20. Yousuf, L.S. Influence of nonlinear dynamics behavior of the roller follower on the contact stress of polydyne cam profile. *Processes* **2022**, *10*, 585. [CrossRef]
21. Zhao, H.; Liu, H.; Xu, J.; Deng, W. Performance prediction using high-order differential mathematical morphology gradient spectrum entropy and extreme learning machine. *IEEE Trans. Instrum. Meas.* **2019**, *69*, 4165–4172. [CrossRef]
22. Zhou, J.; Xiao, M.; Niu, Y.; Ji, G. Rolling bearing fault diagnosis based on WGWOA-VMD-SVM. *Sensors* **2022**, *22*, 6281. [CrossRef] [PubMed]
23. Zeng, Z.; Yang, J.; Wei, Y.; Wang, X.; Wang, P. Fault Detection of Flexible DC Distribution Network Based on GAF and Improved Deep Residual Network. *J. Electr. Eng. Technol.* **2024**, *19*, 3935–3945. [CrossRef]
24. Wang, Z.; Shen, J.; Zhang, X.; Yu, Y.; Wang, Y.; Zhu, H.; Zhang, L. Gear fault diagnosis research based on GAF-TFR-2DCV with small sample size. *Ain Shams Eng. J.* **2025**, *16*, 103344. [CrossRef]
25. Wang, M.; Wang, W.; Zhang, X.; Iu, H.H.-C. A new fault diagnosis of rolling bearing based on Markov transition field and CNN. *Entropy* **2022**, *24*, 751. [CrossRef] [PubMed]
26. Ma, D.; Liu, Z.; Gao, Q.; Yao, J.; Zhao, X.; Zhang, Z. Few-shot fault diagnosis of EHA based on MTF-ResNet-MA and dual-attribute adaptive decision-level fusion. *Measurement* **2025**, *247*, 116787. [CrossRef]
27. Lei, C.; Miao, C.; Wan, H.; Zhou, J.; Hao, D.; Feng, R. Rolling bearing fault diagnosis method based on MTF-MFACNN. *Meas. Sci. Technol.* **2023**, *35*, 035007. [CrossRef]

28. Cong, F.; Chen, J.; Dong, G.; Zhao, F. Short-time matrix series based singular value decomposition for rolling bearing fault diagnosis. *Mech. Syst. Signal Process.* **2013**, *34*, 218–230. [CrossRef]
29. Packard, N.H.; Crutchfield, J.P.; Farmer, J.D.; Shaw, R.S. Geometry from a time series. *Phys. Rev. Lett.* **1980**, *45*, 712. [CrossRef]
30. Takens, F. Detecting strange attractors in turbulence. In *Dynamical Systems and Turbulence, Warwick 1980, Proceedings of a Symposium Held at the University of Warwick 1979/80*; Springer: Berlin/Heidelberg, Germany, 2006; pp. 366–381.
31. Tan, X. Predictive analysis of economic chaotic time series based on chaotic genetics combined with fuzzy decision algorithm. *Complexity* **2021**, *2021*, 5517502. [CrossRef]
32. Li, D.; Cao, M.; Manoach, E.; Ragulskis, M. A novel embedding method for characterization of low-dimensional nonlinear dynamical systems. *Nonlinear Dyn.* **2021**, *104*, 125–148. [CrossRef]
33. Huang, G.; Liu, Z.; Van Der Maaten, L.; Weinberger, K.Q. Densely connected convolutional networks. In Proceedings of the IEEE Conference on Computer Vision and Pattern Recognition, Honolulu, Hawaii, 21–26 July 2017; pp. 4700–4708.

Disclaimer/Publisher's Note: The statements, opinions and data contained in all publications are solely those of the individual author(s) and contributor(s) and not of MDPI and/or the editor(s). MDPI and/or the editor(s) disclaim responsibility for any injury to people or property resulting from any ideas, methods, instructions or products referred to in the content.